Hand–Eye Calibration in Visually-Guided Robot Grinding

Wen-Long Li, He Xie, Gang Zhang, Si-Jie Yan, and Zhou-Ping Yin

Abstract—Visually-guided robot grinding is a novel and promising automation technique for blade manufacturing. One common problem encountered in robot grinding is hand–eye calibration, which establishes the pose relationship between the end effector (hand) and the scanning sensor (eye). This paper proposes a new calibration approach for robot belt grinding. The main contribution of this paper is its consideration of both joint parameter errors and pose parameter errors in a hand–eye calibration equation. The objective function of the hand–eye calibration is built and solved, from which 30 compensated values (corresponding to 24 joint parameters and six pose parameters) are easily calculated in a closed solution. The proposed approach is economic and simple because only a criterion sphere is used to calculate the calibration parameters, avoiding the need for an expensive and complicated tracking process using a laser tracker. The effectiveness of this method is verified using a calibration experiment and a blade grinding experiment. The code used in this approach is attached in the Appendix.

Index Terms—Blade, hand–eye calibration, laser scanning, visually-guided robot grinding.

I. Introduction

BLADES are the most critical parts of aero-engines, nuclear turbines, and coal-power turbines; they come in different sizes and fulfill various roles. Blades function under high temperatures, pressures, and impact loads, and slight changes in their geometry or shape can lead to significant changes in engine performance. To achieve aerodynamic/thermodynamic performance, blades are produced from high-strength and heat-resistant materials (such as super alloy/titanium alloy/austenitic stainless steels) and are designed with thin-walled, crankle, and complex surfaces. A common blade manufacturing process includes forging, deformation correction (primarily originating from thermal transformation or mold wear), milling, grinding, and inspection. Note that grinding is the last machining process in

(a)

(b)

(c)

Fig. 1. Blade parts and a traditional grinding process. (a) Aviation blade (320 mm). (b) Nuclear blade (900 mm). (c) Manual grinding.

generating the blade shape and plays an important role in blade manufacturing quality. Currently, the grinding process is carried out manually by most blade manufacturers [Fig. 1(c)], but grinding is labor intensive and time consuming and the product quality is inconsistent due to poor positional accuracy in manual operation. Most importantly, the dust particles and high-pitched noise encountered in the grinding process can be harmful to human health.

Robot belt grinding is a novel and promising automation technique in blade manufacturing. The grinding system generally includes an industrial robot, a laser scanning sensor, and an abrasive belt. The robot is used to clamp the blade at its end effector and to generate a motion relative to the abrasive belt.

The laser scanning sensor is used to scan and locate the workpiece and to obtain a dense point cloud group, which is used to determine the position and orientation of the blade in the robot basis coordinate frame. Therefore, the grinding procedure can be applied to a workpiece using an efficient matching algorithm. The abrasive belt can be regarded as a tool for cutting off vestige and allowance after milling. Compared with manual grinding, robot grinding has the following advantages: 1) high positional accuracy; 2) flexible contact and broad-line machining; 3) automatic operation; and 4) decreased risk of harm to the operator. Over the past decades, robot belt grinding has been proven as an economic and effective solution for blade grinding [1]–[3]. To grind a workpiece in the current clamping state, the grinding path should be accurately transformed from the workpiece coordinate frame to the basis (or tool) coordinate frame, and the grinding should be performed on a blade that is rigidly fixed at the robot's end effector. In this process, the key is to build the pose relationship between the end effector (hand) and the laser scanning sensor (eye), which is the objective of hand–eye calibration in robot belt grinding. The calibration accuracy influences the homogenization of the grinding allowance and the force, which ultimately determines the surface quality of the blade. Note that the relative pose of the end effector to the scanner varies as a result of changing joint parameters for the robot (primarily the joint angle), which is a typical hand-to-eye calibration problem.

Currently, some calibration methods have been proposed for 3-D inspection, reverse engineering, and machining processes. Traditional robot hand–eye calibration [4], [5] is framed as solving a homogeneous equation $AX = XB$ or $AX = YB$, where X and Y are unknown hand-to-camera and robot-to-world rigid transformations. However, in robot belt grinding, the hand-to-eye transformation is not rigid because the 3-D scanner is not mobile with respect to the robot end effector. Recently, Li *et al.* [6] introduced a hand-to-eye method for a robot scanning system. The camera and the projector of a 3-D scanner were calibrated using a nonlinear approach, and a new tool center point calibration approach was proposed to calibrate the pose from the 3-D scanner to the robot. Ren *et al.* [7] proposed a method to determine the pose between a 3-D scanner and a robot in which the scanner was rigidly mounted on the robot's end effector. The researchers showed that the calibration accuracy approached 0.062 mm. Shi *et al.* [8] developed a robot-aided 3-D inspection system in which a 3-D scanner was mounted on a PUMA 560 robot. The application of 3-D scanner is also found in medical ultrasound inspection [9] and human body tracking [10]. A pixel-to-pixel calibration method was presented to determine sensor parameters. Xu *et al.* [11] proposed a method for self-calibrating a camera's intrinsic parameters using groups of parallel lines; this calibration method was demonstrated using a pose-based visual control experiment using the MOTOMAN robot. Shah [12] introduced a closed-form solution for robot hand–eye calibration using the Kronecker product, and an expensive laser tracker (approximately 200 000 USD) was used to track an active target. Zhan and Wang [13] introduced a hand–eye calibration and positional method for a robot drilling system. This method is simple and practical and can achieve positional accuracy within 0.4 mm. One common problem encountered in these methods is that the hand-to-eye calibration accuracy is greatly limited by the low positional accuracy of the robot, which originates from the geometrical parameters (e.g., link lengths and joint offsets) and predictable deviations (e.g., compliance or gear transmission error). The positional accuracy of a robot can be precalibrated using a laser tracker [14], [15]; however, this approach is expensive.

This paper is motivated by this unsolved problem and aims to propose an economic and simple calibration approach for the application of robot grinding. The approach has two main advantages.

1) This method is economic. Because only a criterion sphere is used to calculate the calibration parameters, the complicated process of tracking correspondences using a laser tracker is not required.
2) This approach is simple. Both joint parameters and pose parameters that require calibration are modeled in a unified objective function and are easily calculated using a least squares strategy.

The remainder of this paper is organized as follows. In Section II, the robot grinding kinematic model is introduced. In Section III, the calibration approach is presented. In Section IV, calibration and quality test experiments are reported to illustrate the availability of the novel approach. The conclusion is presented in Section V.

II. KINEMATIC MODELING

As shown in Fig. 2(a), the grinding path is first generated in the workpiece coordinate frame {W} based on a computer aided design model. To transform the grinding path to an executable program at the current camping state given in Fig. 2(b), one must build the pose relationship from the workpiece coordinate frame to the tool coordinate frame. In Fig. 2(c), we assume that {T, B, E, S} denote the tool coordinate frame, robot basis coordinate frame, end effector coordinate frame, and scanning coordinate frame, respectively. Note that the kinematic equation from the workpiece coordinate frame {W} to the tool coordinate frame {T} is as follows:

$$^T_W T = {}^T_B T \, {}^B_E T \, {}^E_W T \qquad (1)$$

where $^\beta_\alpha T$ denotes a homogeneous transformation matrix from frames {α} to {β}. Note the following symbols.

1) Symbol $^T_B T$ denotes the pose relationship from the robot basis coordinate {B} to the tool coordinate frame {T}, and this matrix can be solved using a linear voltage displacement transducer. Further details can be found in [4].
2) Symbol $^B_E T$ denotes the pose relationship from the end effector coordinate frame {E} to the robot basis coordinate frame {B}. In the application of robot grinding, a 6-DOF joint robot is used, and the initial value (without calibration) of $^B_E T$ can be computed from 24 given joint parameters: $^B_E T = {}^0_6 T = \prod_{i=1}^6 ({}^{i-1}_i T)$, where $^{i-1}_i T$ is an adjacent joint matrix. Coordinate frame {E} is the sixth joint coordinate frame of the robot, and its origin lies at the center of a flange plate. During calibration,
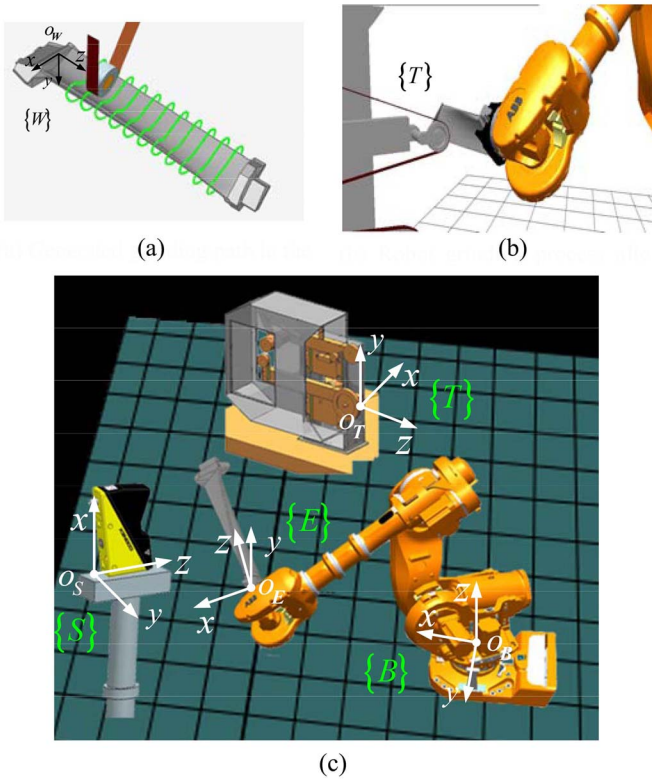
(a)   (b)

(c)

Fig. 2. Kinematic modeling of the hand–eye calibration. (a) Generated grinding path in the workpiece coordinate frame {W}. (b) Robot grinding process after hand–eye calibration. (c) Multicoordinate frames in hand–eye calibration.

a criterion sphere is mounted on the flange plate using a magnetic chuck.

3) Symbol ^E_WT denotes the pose relationship from the workpiece coordinate frame {W} to the end effector coordinate frame {E}. In practice, the blade, which is fixed to the end effector coordinate frame {E}, is scanned by a laser scanner, and the obtained point cloud is registered to the workpiece model in {W} to compute the six transformation parameters in ^E_WT. However, the measured point cloud is directly displayed in {S}, and one has to first build the pose matrix ^S_ET to represent the point cloud in {E}. Therefore, the hand-to-eye calibration matrix ^S_ET is described by the following:

$$^S_ET = ^S_BT^B_ET. \tag{2}$$

The task of hand-to-eye calibration is to determine the two compensated matrices Δ^S_BT and Δ^B_ET with respect to ^S_BT and ^B_ET.

III. CALIBRATION METHOD

The basic principle of calibration is as follows: 1) define the scanning coordinate frame {S} as the world coordinate frame; 2) scan the blade and obtain the measured point ^Sp_j, which is further represented by ^Ep_j in {E}; 3) construct a functional relationship between Δ^Ep (position error) and Δq (calibration parameters); 4) calculate the calibration parameters Δq using a least squares strategy; and 5) calculate the compensated values Δ^S_BT and Δ^B_ET.

A. Principle

Define the homogeneous coordinate of a scanned point in {S} as $^Sp = [^Sp_x, ^Sp_y, ^Sp_z, 1]^T$, then

$$^Ep = \left(^S_ET\right)^{-1}{^Sp}. \tag{3}$$

Actually, there exists

$$^Ep + \Delta^Ep = \left(^S_ET + \Delta^S_ET\right)^{-1}{^Sp} \tag{4}$$

where Δ^Ep is the position error from the theoretical position of ^Ep. Note that the error Δ^Ep originates from Δ^S_ET and that Δ^S_ET originates from both joint parameter errors of $^{i-1}_iT$ and pose parameter errors of ^S_BT. Before calibration, the following functional relationship should first be built:

$$\Delta^Ep = f(\Delta q) \tag{5}$$

where $\Delta q = [\Delta a^T \quad \Delta \alpha^T \quad \Delta d^T \quad \Delta \theta^T \quad D^T_B]^T$ and $\Delta a_{6\times1}, \Delta\alpha_{6\times1}, \Delta d_{6\times1}, \Delta\theta_{6\times1}$ are the parameter errors of the link length, link angle, joint distance, and joint angle, respectively. $D_B = [d^T_B \quad \delta^T_B]^T$ represents the pose parameter errors for ^S_BT, where vector $d_B = [d_{Bx} \quad d_{Bx} \quad d_{Bx}]^T$ is the translation error and vector $\delta_B = [\delta_{Bx} \quad \delta_{By} \quad \delta_{Bz}]^T$ is the axis-angle error.

B. Derivation

In the following, we will give the describing process of ^S_ET and Δ^S_ET. According to the Denavit–Hartenberg (D–H) representation, the homogeneous transformation matrix of two adjacent coordinate frames is

$$^{i-1}_iT(a_{i-1}, \alpha_{i-1}, d_i, \theta_i)$$
$$= \text{Trans}(x, a_{i-1})\text{Rot}(x, \alpha_{i-1})\text{Trans}(z, d_i)\text{Rot}(z, \theta_i) \tag{6}$$

where $\text{Trans}(x, a_{i-1})$, $\text{Trans}(z, d_i)$ are the translation operators along the x- and z-axis and $\text{Rot}(x, \alpha_{i-1})$, $\text{Rot}(z, \theta_i)$ are the rotation operators about the x- and z-axis. The variation of the joint parameter errors is generally small, and the variation of the transformation matrix is approximately equal to its differentials. Therefore, by taking a derivation with respect to the joint parameters $(a_{i-1}, \alpha_{i-1}, d_i, \theta_i)$, one obtains the following:

$$\Delta^{i-1}_iT = \frac{\partial^{i-1}_iT}{\partial a_{i-1}}\Delta a_{i-1} + \frac{\partial^{i-1}_iT}{\partial \alpha_{i-1}}\Delta \alpha_{i-1} + \frac{\partial^{i-1}_iT}{\partial d_i}\Delta d_i + \frac{\partial^{i-1}_iT}{\partial \theta_i}\Delta \theta_i$$
$$= ^{i-1}_iT\Delta_i \tag{7}$$

where Δ_i is the differential operator of the ith joint coordinate frame and is calculated by

$$\begin{bmatrix} 0 & -\Delta\theta_i & -\Delta\alpha_{i-1}s\theta_i & \Delta a_{i-1}c\theta_i - \Delta\alpha_{i-1}d_is\theta_i \\ \Delta\theta_i & 0 & -\Delta\alpha_{i-1}c\theta_i & -\Delta a_{i-1}s\theta_i - \Delta\alpha_{i-1}d_ic\theta_i \\ \Delta\alpha_{i-1}s\theta_i & \Delta\alpha_{i-1}c\theta_i & 0 & \Delta d_i \\ 0 & 0 & 0 & 0 \end{bmatrix}. \tag{8}$$

The symbols c and s are abbreviations for the sine and cosine operators, respectively. Additionally

$$\Delta^S_BT = ^S_BT\Delta_B \tag{9}$$

where $\Delta_B = \begin{bmatrix} 0 & -\delta_{Bz} & \delta_{By} & d_{Bx} \\ \delta_{Bz} & 0 & -\delta_{Bx} & d_{By} \\ -\delta_{By} & \delta_{Bx} & 0 & d_{Bz} \\ 0 & 0 & 0 & 0 \end{bmatrix}$ denotes a differ-

ential operator in coordinate frame {B}. According to (2), (7), and (9), the following exists:

$$\overset{S}{E}T + \Delta\overset{S}{E}T = \overbrace{\left(\overset{S}{B}T + \Delta\overset{S}{B}T\right)}^{\text{Part1}} \bullet \overbrace{\prod_{i=1}^{6}\left(\overset{i-1}{i}T + \Delta\overset{i-1}{i}T\right)}^{\text{Part2}}. \quad (10)$$

Equation (10) builds the relationship between $\Delta\overset{S}{E}T$ and $\Delta\overset{S}{B}T$, $\Delta\overset{i-1}{i}T$, where $\Delta\overset{S}{B}T$ corresponds to the pose parameter errors and $\Delta\overset{i-1}{i}T$ corresponds to the joint parameter errors. By ignoring the second and higher order items in (10), one obtains

$$\Delta\overset{S}{E}T = \overset{S}{B}T\Delta_B\overset{B}{6}T + \overset{S}{B}T\sum_{i=1}^{6}\left(\overset{B}{i}T\Delta_i\overset{i}{6}T\right) \quad (11)$$

where $\overset{B}{6}T$, $\overset{i}{6}T$ denotes the pose relationship from the 6th joint coordinate to basis coordinate frame and the ith joint coordinate, respectively. Because {S} is the world coordinate system, there exists

$$\Delta\overset{S}{E}T = {}^{S}\Delta\overset{S}{E}T \quad (12)$$

where ${}^{S}\Delta = \begin{bmatrix} 0 & -{}^{S}\delta_z & {}^{S}\delta_y & {}^{S}d_x \\ {}^{S}\delta_z & 0 & -{}^{S}\delta_x & {}^{S}d_y \\ -{}^{S}\delta_y & {}^{S}\delta_x & 0 & {}^{S}d_z \\ 0 & 0 & 0 & 0 \end{bmatrix}$ denotes a dif-

ferential operator in {S}. We define a differential motion vector ${}^{S}D = \begin{bmatrix} {}^{S}d^T & {}^{S}\delta^T \end{bmatrix}^T$, where ${}^{S}d = \begin{bmatrix} {}^{S}d_x & {}^{S}d_y & {}^{S}d_z \end{bmatrix}^T$, ${}^{S}\delta = \begin{bmatrix} {}^{S}\delta_x & {}^{S}\delta_y & {}^{S}\delta_z \end{bmatrix}^T$. Applying (6) and (8) to (11), ${}^{S}D$ can be represented by the following:

$$\begin{aligned} {}^{S}D &= \begin{bmatrix} M_a & M_\alpha & M_d & M_\theta & \overset{B}{E}J_1 \\ \mathbf{0}_{3\times6} & N_\alpha & \mathbf{0}_{3\times6} & N_\theta & \overset{B}{E}J_2 \end{bmatrix} \\ &\quad \times \begin{bmatrix} \Delta a^T & \Delta\alpha^T & \Delta d^T & \Delta\theta^T & D_B{}^T \end{bmatrix}^T \\ &= G_{6\times30}\Delta q_{30\times1} \end{aligned} \quad (13)$$

where $M_\gamma(\gamma = a, \alpha, d, \theta)$ is a 3×6 matrix and denotes the influence of the joint parameter errors on ${}^{S}d \cdot N_\gamma(\gamma = \alpha, \theta)$ is also a 3×6 matrix and denotes the influence of the joint parameter errors on ${}^{S}\delta \cdot \overset{B}{E}J = [\overset{B}{E}J_1^T \quad \overset{B}{E}J_2^T]^T$ is a 6×6 Jacobian matrix and denotes the influence of the pose parameter errors D_B on ${}^{S}D$.

C. Identification

Equation (13) builds a functional relationship between the calibration parameters Δq and the motion vector ${}^{S}D$, which is used to calculate Δq. For an observed point ^Ep_j, according to (4), (13), and (33), there exists

$$^Ep_j + \Delta^Ep_j = {}^Ep_j + \overset{S}{E}R_j^T\left[-I\ S(^Sp_j)\right]G_j\Delta q. \quad (14)$$

The details can be found in Appendix A. Then

$$\Delta^Ep_j = K_j\Delta q \quad (15)$$

where $K_j = \overset{S}{E}R_j^T\left[-I\ S(^Sp_j)\right]G_j$. Note that (15) builds the functional relationship between Δq and Δ^Ep in (5). In an experiment, the theoretical position of the observed point ^Ep_j is unchanged for a pair of scans. Then

$$^Ep_1 + K_1\Delta q = {}^Ep_2 + K_2\Delta q \quad (16)$$

and $(K_1 - K_2)\Delta q = ^Ep_2 - {}^Ep_1$. Because there are 30 unknown parameters in (13), $n(n \geq 30)$ pairs of scans are required. Then

$$\begin{bmatrix} K_{11} - K_{12} \\ K_{21} - K_{22} \\ \ldots \\ K_{n1} - K_{n2} \end{bmatrix}\Delta q = \begin{bmatrix} ^Ep_{12} - {}^Ep_{11} \\ ^Ep_{22} - {}^Ep_{21} \\ \ldots \\ ^Ep_{n2} - {}^Ep_{n1} \end{bmatrix} \quad (17)$$

and

$$A\Delta q = B. \quad (18)$$

Therefore, the joint parameter errors and pose parameter errors that must be calibrated are $\Delta q = (A^TA)^{-1}A^TB = A^+B$.

According to (9) and (13), the compensated value $\Delta\overset{S}{B}T$ is

$$\Delta\overset{S}{B}T = \overset{S}{B}T\begin{bmatrix} S(D_B(4:6)) & D_B(1:3) \\ \mathbf{0}_{1\times3} & 0 \end{bmatrix} \quad (19)$$

where $S()$ denotes anti-symmetry and $D_B = \Delta q(25:30)$.

Similarly, according to (12) and (13), the compensated value $\Delta\overset{B}{E}T$ is the following:

$$\Delta\overset{S}{E}T = \begin{bmatrix} S({}^SD(4:6)) & {}^SD(1:3) \\ \mathbf{0}_{1\times3} & 0 \end{bmatrix}\overset{S}{E}T. \quad (20)$$

D. Initial Value

Note that an initial value of $\overset{S}{B}T$ should be determined before the calculation in (18) is performed. Because $^Ep_j = \overset{E}{S}T_j^S p_j = \overset{E}{B}T_j\overset{B}{S}T^Sp_j$, there exists

$$^Ep_j = \overset{E}{B}R_j\left(\overset{B}{S}R^Sp_j + {}^Bp_{So}\right) + {}^Ep_{Boj} \quad (21)$$

where $\overset{E}{B}T_j = \begin{bmatrix} \overset{E}{B}R_j & ^Ep_{Boj} \\ \mathbf{0}_{1\times3} & 1 \end{bmatrix}$ and $\overset{B}{S}T = \begin{bmatrix} \overset{B}{S}R & {}^Bp_{So} \\ \mathbf{0}_{1\times3} & 1 \end{bmatrix}$. $^Ep_{Boj}$ denotes the origin position of {B} in {E}, and $^Bp_{So}$ denotes the origin position of {S} in {B}. After employing a vectorization operator, one obtains the following:

$$\begin{aligned} ^Ep_j &= \begin{bmatrix} \text{Vec}\left({}^Sp_j^T \otimes \overset{E}{B}R_j\right) & \overset{E}{B}R_j \end{bmatrix}\begin{bmatrix} \text{Vec}\left(\overset{B}{S}R\right) \\ {}^Bp_{So} \end{bmatrix} + {}^Ep_{Boj} \\ &= M_jX + {}^Ep_{Boj} \quad (j = 1, 2). \end{aligned} \quad (22)$$

When $m(m \geq 12)$ pairs of scans are performed, there exists

$$\begin{bmatrix} M_{11} - M_{12} \\ M_{21} - M_{22} \\ \ldots \\ M_{m1} - M_{m2} \end{bmatrix}X = \begin{bmatrix} ^Ep_{Bo12} - {}^Ep_{Bo11} \\ ^Ep_{Bo22} - {}^Ep_{Bo21} \\ \ldots \\ ^Ep_{Bom2} - {}^Ep_{Bom1} \end{bmatrix}. \quad (23)$$

The simplified equation is $CX = D$, and

$$X = (C^TC)^{-1}C^TD. \quad (24)$$

Therefore, the posture $\overset{B}{S}R$ and the position $^Bp_{So}$ in $\overset{S}{B}T$ can be calculated by (24). Furthermore

$$\overset{B}{S}R = [X(1:3), X(4:6), X(7:9)], {}^Bp_{So} = X(10:12). \quad (25)$$

To guarantee the orthogonality of matrix $^B_S R$, Gram–Schmidt algorithm can be used. After that, matrix $^S_B T$ is

$$^S_B T = \begin{bmatrix} ^B_S R & ^B p_{So} \\ \mathbf{0}_{1\times 3} & 1 \end{bmatrix}^{-1}. \tag{26}$$

IV. EXPERIMENTS AND ANALYSIS

In the following, the proposed hand–eye calibration approach is carried out to verify the calibration results when applied to robot belt grinding. In the following experiments, an ABB IRB6650S industrial robot was used to grind a nuclear blade with a length of 905 mm, and a portable Cognex DS1000 3-D scanner was mounted on the ground for scanning and calibration. The main technical parameters of the robot, the scanner, and the abrasive belt are as follows.

1) *Robot:*
   a) position repeatability: 0.11 mm;
   b) handing capacity: 125 kg;
   c) reach range: 3.5 m.
2) *3-D Scanner:*
   a) resolution (Z): 0.007–0.040 mm;
   b) resolution (X): 0.07–0.15 mm;
   c) field of view: 120–175 mm.
3) *Abrasive Belt:*
   a) ceramic abrasive belt for rough/finish grinding, with a grain number of 120 and 240;
   b) the linear velocity of the contact wheel was 18.3 and 5.6 m/s.

A. Calibration Verification

As shown in Fig. 3(a), a criterion sphere ($d_{given} = 60$ mm) was mounted on the robot's end effector and was scanned from 40 different poses (corresponding to 40 pairs of data). The obtained point cloud for each scan was approximated to generate a sphere model using a least squares strategy. For each pair of scans, the point cloud corresponds to a pair of $(^B_E T_{j1}, ^S p_{j1})$, $(^B_E T_{j2}, ^S p_{j2})$. Applying 40 pairs of $(^B_E T_{j1}, ^S p_{j1})$, $(^B_E T_{j2}, ^S p_{j2})$ to (24), the variable X in (24) is calculated, and an initial value of $^S_B T$ is calculated using the following:

$$^S_B T_0 = \begin{bmatrix} 0.989994 & 0.1392368 & 0.022895 & -1036.4696 \\ -0.018769 & -0.030873 & 0.999347 & -1546.252 \\ 0.139852 & -0.989778 & -0.02795 & 1537.0817 \\ 0 & 0 & 0 & 1 \end{bmatrix}.$$

Using $^S_B T_0$, $(^B_E T_{j1}, ^S p_{j1})$, $(^B_E T_{j2}, ^S p_{j2})$, and the theoretical parameters of the ABB robot (Table I), the values of the calibrated parameters $\Delta q_{30\times 1}$ can be calculated by (18). Note that $\Delta q_{30\times 1}$ includes 24 compensated values $\begin{bmatrix} \Delta a^T & \Delta \alpha^T & \Delta d^T & \Delta \theta^T \end{bmatrix}^T$ corresponding to the joint parameters in Table II and six compensated values D_B corresponding to the matrix $^S_B T$:
$$D_B = \begin{bmatrix} 0.1430 & 0.9352 & 0.8467 & -0.0019 & 0.0014 & 0.0023 \end{bmatrix}^T.$$
Then, the anti-symmetric matrix from D_B is

$$\Delta_B = \begin{bmatrix} 0 & -0.0023 & 0.0014 & 0.1430 \\ 0.0023 & 0 & 0.0019 & 0.9352 \\ -0.0014 & -0.0019 & 0 & 0.8467 \\ 0 & 0 & 0 & 0 \end{bmatrix}, \text{ and}$$
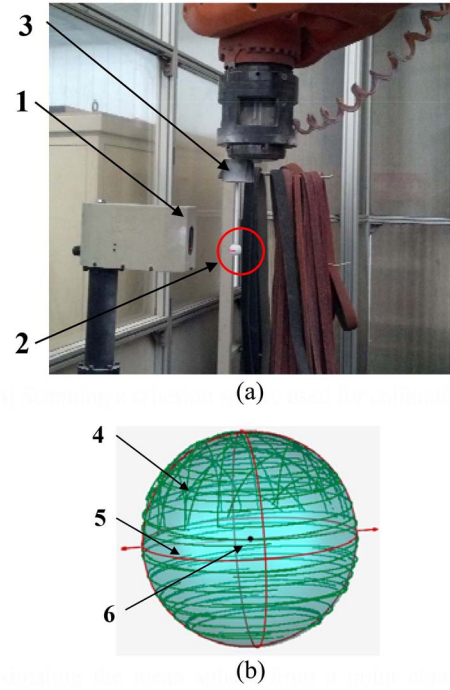

(a)

(b)

Fig. 3. Hand–eye calibration process. 1) Laser scanner. 2) Criterion sphere. 3) Magnetic sucker. 4) Scanning lines (green). 5) Approximated mean sphere (red). 6) Sphere center (black). (a) Scanning a criterion sphere used for calibration. (b) Approximating the mean sphere from a point cloud using the compensated parameter errors.

TABLE I
ABB IRB6650S JOINT PARAMETERS

i th joint	a_{i-1} (mm)	α_{i-1} (rad)	d_i (mm)	θ_i (rad)	Range of θ_i (rad)
1	0	0	630	0	$-\pi \sim +\pi$
2	600	$-\pi/2$	0	$-\pi/2$	$-0.2222\,\pi \sim +0.8889\,\pi$
3	1280	0	0	0	$-\pi \sim +0.3889\,\pi$
4	200	$-\pi/2$	1592	π	$-1.6667\,\pi \sim +1.6667\,\pi$
5	0	$-\pi/2$	0	0	$-0.6667\,\pi \sim +0.6667\,\pi$
6	0	$\pi/2$	200	0	$-2\,\pi \sim +2\,\pi$

its corresponding $\Delta^S_B T$ is calculated using (19). The updated $^S_B T$ after adding $\Delta^S_B T$ is as follows:

$$^S_B T = \begin{bmatrix} 0.990283 & 0.136911 & 0.024546 & -1036.1785 \\ -0.020239 & -0.032728 & 0.999262 & 1545.4377 \\ 0.137615 & -0.990046 & -0.029635 & 1536.1524 \\ 0 & 0 & 0 & 1 \end{bmatrix}.$$

Using the calculated $^S_B T$ and $\Delta q_{30\times 1}$, the compensated $\Delta^S_E T$ can be calculated by (20), and the positions of 80 approximated sphere centers are updated using (4). The mean value of the sphere center coordinate is $c_{compensated} = (-32.1926, 16.5602, 367.7075)^T$ mm, and the diameter of the approximated mean sphere from all scanning lines is

TABLE II
COMPENSATED VALUES OF JOINT PARAMETERS FOR ABB IRB6650S

i th joint	Δa_{i-1} (mm)	$\Delta \alpha_{i-1}$ (rad)	Δd_i (mm)	$\Delta \theta_i$ (rad)
1	0.0006	-0.0017	0.3310	-0.0035
2	0.2187	0.0036	0.0024	0.0000
3	0.6428	0.0001	0.0000	0.0015
4	0.1279	0.0028	0.4710	0.0023
5	0.0000	0.0003	0.0010	-0.0007
6	0.0016	-0.0018	0.2042	0.0102

TABLE III
CALCULATED RESULTS FOR THE TWO CALIBRATION METHODS

Coordinate	Real value (mm)	Reference [6] (mm)	Our method (mm)
X	-35.0000	-35.1013	-34.9568
Y	17.0000	17.2442	16.9489
Z	360.0000	360.0160	360.0065
Diameter deviation e	——	**0.2646 mm**	**0.0672 mm**

$\bar{d}_{\text{compensated}} = 59.9534$ mm. The graphical result of the generated sphere with its mean diameter is shown in Fig. 3(b). The diameter deviation of the mean sphere with respect to the criterion sphere is

$$e = \left| \bar{d}_{\text{compensated}} - d_{\text{given}} \right| = 0.0466 \text{ mm}. \tag{27}$$

The distance deviations of the mean sphere center to each approximated sphere center are

$$e_{\text{max}+} = 0.1933 \text{ mm}, e_{\text{max}-} = -0.1551 \text{ mm}, e_{\text{std}} = 0.0254 \text{ mm}. \tag{28}$$

For the approximated sphere without compensation, the mean value of the sphere center coordinate is $c' = (-32.1897, 16.6479, 367.7479)$ mm, and the diameter of the approximated mean sphere is $\bar{d}_{\text{uncompensated}} = 60.1493$ mm. Accordingly, the diameter deviation and distance deviation are

$$e' = \left| \bar{d}_{\text{uncompensated}} - d_{\text{given}} \right| = 0.1493 \text{ mm}$$
$$e'_{\text{max}+} = 0.9215 \text{ mm}, e'_{\text{max}-} = -0.9932 \text{ mm}$$
$$e'_{\text{std}} = 0.0789 \text{ mm}. \tag{29}$$

The diameter deviation and the distance deviation are thus reduced after performing the calibration described in Section III. The diameter deviation after calibration was only 0.0466 mm.

Additionally, we compared our method with a similar hand-to-eye calibration method introduced in [6]. We set the real value of the sphere center coordinate to $^E\boldsymbol{p} = (-35.0000, 17.0000, 360.0000)^T$ mm, and the real value of the basis coordinate frame to the scanning coordinate frame was

$$^S_B T = \begin{bmatrix} 0.9901172 & 0.1388261 & 0.0198782 & -1036.0000 \\ -0.0172825 & -0.019878 & 0.9996530 & 1545.0000 \\ 0.1391731 & -0.9901172 & -0.0172825 & 1536.0000 \\ 0 & 0 & 0 & 1 \end{bmatrix},$$

where the rotation vector is $\begin{bmatrix} \alpha & \beta & \gamma \end{bmatrix} = \begin{bmatrix} -91^o & -8^o & -1^o \end{bmatrix}^T$ and the translation vector is $\begin{bmatrix} p_x & p_y & p_z \end{bmatrix}^T = \begin{bmatrix} -1036 & 1545 & 1536 \end{bmatrix}^T$ mm. In the following experiment, 100 pairs of $\Gamma_1 = \{^B_E T_{j1}\}, \Gamma_2 = \{^B_E T_{j2}\}, j = 1, \ldots, 100$ were generated over angle θ_i, which is given in Table I. According to the requirements for the calibration method in [6], each pair of $^B_E T_{j1}, ^B_E T_{j2}$ has the same posture but a different position. Then, 100 pairs of ideal $\Pi_1 = \{^S P_{j1}\}, \Pi_2 = \{^S P_{j2}\}$ were obtained with $^S P_{j1} = ^S_B T ^B_E T_{j1} ^E \boldsymbol{p}, ^S P_{j2} = ^S_B T ^B_E T_{j2} ^E \boldsymbol{p}$. Due to the presence of

(a)

(b)   (c)

Fig. 4. Nuclear blade grinding experiment. (a) Robot belt grinding process. (b) After robot grinding. (c) After manual grinding.

robot joint parameter errors, the compensated values in Table II were used to generate another 100 pairs of Γ'_1, Γ'_2.

According to Π_1, Π_2, and Γ'_1, Γ'_2, the matrix $^S_B T$ and the sphere's center coordinate are calculated using [6]. Correspondingly, the matrix $^S_B T$ and the sphere center coordinates are also calculated using our calibration method given in (14), (15), (18), and (25). The calculated results are shown in Table III. The diameter deviation is 0.2646 mm versus 0.0672 mm, indicating that the proposed calibration method is relatively accurate and that both joint parameter errors $^B_E T$ and pose parameter errors $^S_B T$ can be easily calculated in a closed solution.
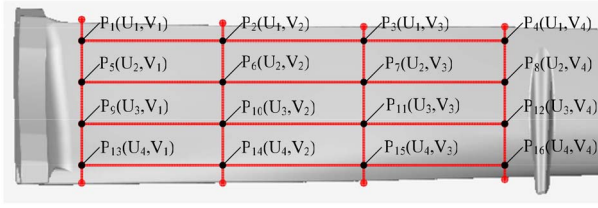
Fig. 5. Observed surface roughness point layout.

TABLE IV
SURFACE ROUGHNESS OBTAINED FOR ROBOT GRINDING (R_a/μm)

	V1	V2	V3	V4	Mean value	Standard deviation
U1	0.249	0.302	0.265	0.263	0.270	0.023
U2	0.231	0.236	0.314	0.242	0.256	0.039
U3	0.262	0.286	0.238	0.332	0.280	0.040
U4	0.274	0.218	0.212	0.270	0.244	0.033
Mean value	0.254	0.261	0.257	0.277	**0.262**	
Standard deviation	0.018	0.040	0.044	0.039		**0.034**

TABLE V
SURFACE ROUGHNESS OBTAINED FOR MANUAL GRINDING (R_a/μm)

	V1	V2	V3	V4	Mean value	Standard deviation
U1	0.783	0.679	0.420	0.483	0.591	0.169
U2	0.552	0.491	0.629	0.840	0.628	0.152
U3	0.658	0.650	0.640	0.567	0.629	0.042
U4	0.696	0.632	0.607	0.642	0.644	0.038
Mean value	0.672	0.613	0.574	0.633	**0.623**	
Standard deviation	0.096	0.084	0.104	0.154		**0.107**

B. Grinding Quality Verification

In the second experiment, a nuclear blade was mounted on the robot's end effector using a special fixture and was scanned using a laser scanner [shown in Fig. 4(a)]. Using the hand–eye calibration results from Section IV-A, the obtained point cloud was represented in the end effector coordinate frame {E} and was subsequently registered to the blade model in the workpiece frame {W}. Therefore, the calculated registering parameters, which include three rotation parameters and three translation parameters, are used to translate the grinding procedure for the current blade clamping state. The blade after robot grinding is shown in Fig. 4(b).

To verify the robot grinding quality, the manually ground part shown in Fig. 4(c) was used for comparison. In Fig. 5,

16 observed points (P1–P16) in the design model were selected to measure the surface roughness. The observed values are given in Tables IV and V. The mean surface roughness (16 observed points) for the robot grinding was 0.262 μm, which is much less than the mean value for the manual grinding (0.623 μm). The mean standard deviation for the robot grinding was only 0.034 μm, which is also much less than the mean value for the manual grinding (0.107 μm). This result shows that the proposed hand–eye calibration approach described in Section III is effective and that the grinding surface quality is better than that obtained via manual grinding.

V. CONCLUSION

This paper addresses the hand–eye calibration problem from a robot's end effector to the laser scanning sensor. The kinematic equation for the robot grinding is built using homogeneous transformation matrices, from which the task of hand–eye calibration is given: compensating 24 joint parameter errors for $_E^B T$ and six pose parameter errors for $_B^S T$. Subsequently, the relationship between the position error $\Delta^E \boldsymbol{p}$ of the observed point and the parameter errors $\Delta \boldsymbol{q}$ is built using a D–H matrix and differential derivation. Then, the parameter errors $\Delta \boldsymbol{q}_{30 \times 1}$ that must be calibrated are calculated using a least squares strategy. This calibration approach is economic and simple to implement because only a criterion sphere is used. More importantly, the joint parameter errors and the pose parameter errors are uniformly modeled and calculated; thus, the need for an expensive and complicated tracking process using a laser tracker, which is traditionally utilized, is avoided. In the calibration experiment, the diameter deviation after calibration was reduced to 0.0466 mm versus 0.1493 mm. The mean surface roughness for the robot grinding was found to be smaller than that for manual grinding: 0.262 μm versus 0.623 μm. The proposed calibration approach can be used extensively in the robot grinding of nuclear blades, aviation blades, and turbine blades, but it is best to use blades with a length of less than 1200 mm, given the rigidity of the robot grinding system.

APPENDIX A
PROOF OF $\Delta^E \boldsymbol{p}_j = K_j \Delta \boldsymbol{q}$

Given

$$\Delta_E^S T = {}^S \Delta_E^S T \tag{30}$$

where symbol ${}^S \Delta$ is a matrix of differential operators and denotes the pose error of the robot end effector origin Eo to {S}. ${}^S \Delta$ can be represented by

$$
{}^S \Delta = \begin{bmatrix} 0 & -{}^S \delta_z & {}^S \delta_y & {}^S d_x \\ {}^S \delta_z & 0 & -{}^S \delta_x & {}^S d_y \\ -{}^S \delta_y & {}^S \delta_x & 0 & {}^S d_z \\ 0 & 0 & 0 & 0 \end{bmatrix} = \begin{bmatrix} S({}^S \boldsymbol{\delta}) & {}^S \boldsymbol{d} \\ \boldsymbol{0}_{1 \times 3} & 0 \end{bmatrix} \tag{31}
$$

where $S({}^S \boldsymbol{\delta})$ is an anti-symmetric matrix corresponding to ${}^S \boldsymbol{\delta} = \begin{bmatrix} {}^S \delta_x & {}^S \delta_y & {}^S \delta_z \end{bmatrix}^T$. If one ignores the second or higher

$$\begin{bmatrix} {}^E\boldsymbol{p} + \Delta^E\boldsymbol{p} \\ 1 \end{bmatrix} = \left({}^S_E T + \Delta_S {}^S_E T \right)^{-1} \begin{bmatrix} {}^S\boldsymbol{p} \\ 1 \end{bmatrix}$$

$$= \left(\begin{bmatrix} {}^S_E R & {}^S\boldsymbol{p}_{Eo} \\ 0 & 1 \end{bmatrix} + \begin{bmatrix} S({}^S\boldsymbol{\delta}) & {}^S\boldsymbol{d} \\ 0 & 1 \end{bmatrix} \begin{bmatrix} {}^S_E R & {}^S\boldsymbol{p}_{Eo} \\ 0 & 1 \end{bmatrix} \right)^{-1} \begin{bmatrix} {}^S\boldsymbol{p} \\ 1 \end{bmatrix}$$

$$= \begin{bmatrix} {}^S_E R^T \left(I + S({}^S\boldsymbol{\delta})^T \right) & -{}^S_E R^T \left(I + S({}^S\boldsymbol{\delta})^T \right) \left({}^S\boldsymbol{p}_{Eo} + S({}^S\boldsymbol{\delta}){}^S\boldsymbol{p}_{Eo} + {}^S\boldsymbol{d} \right) \\ 0 & 1 \end{bmatrix} \begin{bmatrix} {}^S\boldsymbol{p} \\ 1 \end{bmatrix}$$

$$\approx \begin{bmatrix} {}^S_E R^T \left(I + S({}^S\boldsymbol{\delta})^T \right) & -{}^S_E R^T \left({}^S\boldsymbol{p}_{Eo} + {}^S\boldsymbol{d} \right) \\ 0 & 1 \end{bmatrix} \begin{bmatrix} {}^S\boldsymbol{p} \\ 1 \end{bmatrix}. \tag{32}$$

order items, there exists (32), as shown at the top of this page. Then, in a pair of scans, there exists

$$\begin{aligned} {}^E\boldsymbol{p}_j + \Delta^E\boldsymbol{p}_j &= {}^S_E R_j^T \left(I + (S({}^S\boldsymbol{\delta}))^T \right) {}^S\boldsymbol{p}_j - {}^S_E R_j^T \left({}^S\boldsymbol{p}_{Eoj} + {}^S\boldsymbol{d} \right) \\ &= {}^S_E R_j^T \left({}^S\boldsymbol{p}_j - {}^S\boldsymbol{p}_{Eoj} + S({}^S\boldsymbol{p}_j){}^S\boldsymbol{\delta} - {}^S\boldsymbol{d} \right) \\ &= {}^S_E R_j^T \left({}^S\boldsymbol{p}_j - {}^S\boldsymbol{p}_{Eoj} + \left[-I \ S({}^S\boldsymbol{p}_j) \right] \left[{}^S\boldsymbol{d}^T \ {}^S\boldsymbol{\delta}^T \right]^T \right) \\ &= {}^S_E R_j^T \left({}^S\boldsymbol{p}_j - {}^S\boldsymbol{p}_{Eoj} \right) + {}^S_E R_j^T \left[-I \ S({}^S\boldsymbol{p}_j) \right] {}^S\boldsymbol{D} \\ &= {}^E\boldsymbol{p}_j + {}^S_E R_j^T \left[-I \ S({}^S\boldsymbol{p}_j) \right] G_j \Delta\boldsymbol{q} \\ &= {}^E\boldsymbol{p}_j + K_j \Delta\boldsymbol{q} \quad (j = 1, 2). \end{aligned} \tag{33}$$

Therefore, $\Delta^E\boldsymbol{p}_j = K_j \Delta\boldsymbol{q}$.

APPENDIX B
MATLAB CODE FOR HAND–EYE CALIBRATION
(MAIN PROGRAM)

```
% Definition of three nested functions and coordinate frames
% Fkine: Kinematics positive solution of robot
% CalK: Calculate Ki in (16)
% Antisymmetric: Construct anti-symmetric matrix
% Coordinate frames: b-{B}, s-{S}, e-{E}

% Initialization:
Close all; Clear all
Q=[0 0 630 0; 600 -1/2*pi 0 -1/2*pi; 1280 0 0 0;
    200 -1/2*pi 1592 pi; 0 1/2*pi 0 0; 0 1/2*pi 200 0];

% Given Joint parameters in Table I
Ps1; Ps2;                          % Point cloud (3*nPt) in {S}
Tbe1; Tbe2;   % Pose matrix (4*4*nPt) of frame {B} to {e}
Theta1; Theta2;                    % Joint angles (6*nPt)

% Step1: Calculate pose Tbs of {B} to {S}
nPt=size(Ps1,2);
C=zeros(3*nPt,12);                 % Matrix C in Eq.(22)
D=zeros(3*nPt,1);                  % Matrix D in Eq.(22)
for i=1:nPt
  Rbe1=inv(E1(1:3,1:3,i));         % Rbe1 in Eq.(3)
  Rbe2=inv(E2(1:3,1:3,i));         % Rbe2 in Eq.(3)
  M1i=[kron(Ps1(:,i)', Rbe1)), Rbe1];   % Mi1 in Eq.(21)
  M2i=[kron(Ps2(:,i)', Rbe2)), Rbe2];   % Mi2 in Eq.(21)
```

```
  Pbo1i=Tbe1(1:3,4,i);             % Pbo1i in Eq.(21)
  Pbo2i= Tbe2(1:3,4,i)             % Pbo2i in Eq.(21)
  C(3*i-2:3*i,:)=M1i-M2i;          % Matrix C in Eq.(22)
  D(3*i-2:3*i,1)= Pbo2i - Pbo1i;   % Matrix D in% Eq.(22)
end
X=inv(dM'*dM)*dM'*dPbe;            % Eq.(22)
Tbs=[X(1:3,1),X(4:6,1),X(7:9,1),X(10:12,1);0 0 0 1] % Eq.(23)

% Step2: Calculate dq
A=zeros(3*nPt,30);                 % Matrix A in Eq.(18)
B=zeros(3*nPt,1);                  % Matrix B in Eq.(18)
for i=1:nPt
    T1i=inv(Tbs*E1(:,:,i)); T2i=inv(Tbs*E2(:,:,i));  % Eq.(3)
    Q1i=[Q(:,1:3),Theta1(:,i)]; Q2i=[Q(:,1:3), Theta2(:,i)];
                                   % Update joint parameters
  K1i=CalK(Q1i, Tbs,Ps1(:,i));     % Ki1 in Eq.(17)
  K2i=CalK(Q2i, Tbs,Ps2(:,i));     % Ki2 in Eq.(17)
  Pe1i=T1i(1:3,1:3)*Ps1(:,i)+T1i(1:3,4);     % Pei1 Eq.(17)
  Pe2i=T2i(1:3,1:3)*Ps2(:,i)+T2i(1:3,4);     % Pei2 Eq.(17)
  A(3*i-2:3*i,:)=K1i-K2i;          % A in Eq.(18)
  B(3*i-2:3*i,1)=Pe2i-Pe1i;        % B in Eq.(18)
end
dq=inv(A'*A)*A'*B;                 % dq in Eq.(18)

% Step3: Compensation
dQ=[dq(1:6),dq(7:12),dq(13:18),dq(19:24)];
                                   % Compensated value of Q
DetaTbs=Tbs*[Antisymmetric(dq(25:27,:)),dq(28:30,:);0 0 0 1];
                                   % DeltaTbs in Eq.(10)
CpsTbs=Tbs+DetaTbs;                % Compensate Tbs
CpsQ=Q+dQ;                         % Compensate Q
CpsTbe1=zeros(4,4,nPt);            % E1 after compensation
CpsTbe2=zeros(4,4,nPt);            % E2 after compensation
CpsPe1=zeros(4,nPt);              % Pe1 after compensation
CpsPe2=zeros(4,nPt);              % Pe2 after compensation
for i= 1:nPt
    CpsQi1=[CpsQ(:,1:3),Theta1(:,i)+dQ(:,4)];
    CpsQi2=[CpsQ(:,1:3),Theta2(:,i)+dQ(:,4)];
                                   % Update joint parameters by dQ
    CpsTbe1(:,:,i)=Fkine(CpsQi1);
    CpsTbe2(:,:,i)=Fkine(CpsQi2);
                                   % Kinematics positive solution
    CpsPe1(:,i)=inv(CpsTbs*CpsTbe1(:,:,i))*[Ps1(:,i);1];
    CpsPe2(:,i)=inv(CpsTbs*CpsTbe2(:,:,i))*[Ps2(:,i);1];
                                   % Eq.(4)
end
```

```
CpsPe1=CpsPe1(1:3,:);
CpsPe2=CpsPe2(1:3,:);
Scatter3(CpsPe1(1,:), CpsPe1(2,:), CpsPe1(3,:));
Scatter3(CpsPe2(1,:), CpsPe2(2,:), CpsPe2(3,:));
          % Output updated coordinate in citation{E}
```
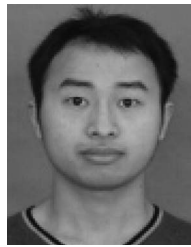
REFERENCES

[1] H. Huang, Z. M. Gong, X. Q. Chen, and L. Zhou, "SMART robotic system for 3D profile turbine vane airfoil repair," *Int. J. Adv. Manuf. Technol.*, vol. 21, no. 4, pp. 275–283, 2003.

[2] X. Ren, M. Cabaravdic, X. Zhang, and B. Kuhlenkötter, "A local process model for simulation of robotic belt grinding," *Int. J. Mach. Tools Manuf.*, vol. 47, no. 6, pp. 962–970, 2007.

[3] Y. Q. Sun, D. J. Giblin, and K. Kazerounian, "Accurate robotic belt grinding of workpieces with complex geometries using relative calibration techniques," *Robot. Comput. Integr. Manuf.,* vol. 25, no. 1, pp. 204–210, 2009.

[4] C.-C. Wang, "Extrinsic calibration of a vision sensor mounted on a robot," *IEEE Trans. Robot. Autom.*, vol. 8, no. 2, pp. 161–175, Apr. 1992.

[5] F. Dornaika and R. Horaud, "Simultaneous robot-world and hand-eye calibration," *IEEE Trans. Robot. Autom.,* vol. 14, no. 4, pp. 617–622, Aug. 1998.

[6] J. F. Li *et al.,* "Calibration of a portable laser 3-D scanner used by a robot and its use in measurement," *Opt. Eng.,* vol. 47, no. 1, pp. 1–8, 2008.

[7] Y. J. Ren, S. B. Yin, and J. G. Zhu, "Calibration technology in application of robot-laser scanning system," *Opt. Eng.,* vol. 51, no. 11, 2012, Art. ID 114204.

[8] Q. Shi, N. Xi, and C. Zhang, "Develop a robot-aided area sensing system for 3D shape inspection," *ASME J. Manuf. Sci. Eng.,* vol. 132, no. 1, 2010, Art. ID 014502.

[9] Q. H. Huang *et al.,* "Linear tracking for 3-D medical ultrasound imaging," *IEEE Trans. Cybern.*, vol. 43, no. 6, pp. 1747–1754, Dec. 2013.

[10] O. S. Gedik and A. A. Alatan, "3-D rigid body tracking using vision and depth sensors," *IEEE Trans. Cybern.,* vol. 43, no. 5, pp. 1395–1405, Oct. 2013.

[11] D. Xu, Y. F. Li, Y. Shen, and M. Tan, "New pose-detection method for self-calibrated cameras based on parallel lines and its application in visual control system," *IEEE Trans. Syst., Man, Cybern. B, Cybern.,* vol. 36, no. 5, pp. 1104–1117, Oct. 2006.

[12] M. Shah, "Solving the robot-world/hand-eye calibration problem using the Kronecker product," *ASME J. Mach. Robot.*, vol. 5, no. 3, 2013, Art. ID 031007.

[13] Q. Zhan and X. Wang, "Hand-eye calibration and positioning for a robot drilling system," *Int. J. Adv. Manuf. Technol.,* vol. 61, nos. 5–8, pp. 691–701, 2012.

[14] C. Gong, J. Yuan, and J. Ni, "Nongeometric error identification and compensation for robotic system by inverse calibration," *Int. J. Mach. Tools Manuf.,* vol. 40, no. 14, pp. 2119–2137, 2000.

[15] A. Nubiola and I. A. Bonev, "Absolute calibration of an ABB IRB 1600 robot using a laser tracker," *Robot. Comput. Integr. Manuf.,* vol. 29, no. 1, pp. 236–245, 2013.

He Xie received the B.S. degree in mechatronic engineering from the Huazhong University of Science and Technology, Wuhan, China, in 2012, where he is currently pursuing the Ph.D. degree.

His current research interests include laser scanning.

Gang Zhang received the B.S. degree in mechatronic engineering from the Shandong University of Science and Technology, Tai'an, China, in 1996, the M.S. degree in mechanical engineering from the Beijing University of Aeronautics and Astronautics, Beijing, China, in 2002, and the Ph.D. degree in mechanical engineering from Shanghai Jiao Tong University, Shanghai, China, in 2014.

He is currently a Post-Doctoral Research Fellow with the Huazhong University of Science and Technology, Wuhan, China. His current research interests include robotic grinding and motion control of robots.

Si-Jie Yan received the Ph.D. degree in mechatronic engineering from the Huazhong University of Science and Technology (HUST), Wuhan, China, in 1997.

He is currently an Associate Professor with the State Key Laboratory of Digital Manufacturing Equipment and Technology, HUST. His current research interests include blade machining and robot grinding.

Wen-Long Li received the B.S. degree in mechanical engineering and automation from Xi'an Jiaotong University, Xi'an, China, in 2004, and the Ph.D. degree in mechatronic engineering from the Huazhong University of Science and Technology (HUST), Wuhan, China, in 2010.

He is currently an Associate Professor with the State Key Laboratory of Digital Manufacturing Equipment and Technology, HUST. His current research interests include robot grinding and visual inspection of blades.

Zhou-Ping Yin received the B.S. and Ph.D. degrees in mechatronic engineering from the Huazhong University of Science and Technology (HUST), Wuhan, China, in 1994 and 2000, respectively.

From 2000 to 2002, he was a Post-Doctoral Research Fellow with the HUST, and in 2002, he was an Associate Professor with the HUST. Since 2004, he has been a Professor with the State Key Laboratory of Digital Manufacturing Equipment and Technology, HUST, where he is currently a Cheung Kong Chair Professor. His current research interests include electronics manufacturing, digital manufacturing, and geometric reasoning.